RADAR System for Sense and Mapping in Small Air Vehicles

Nuno Filipe Paquim Soares Brandão
nunofsbrandao@tecnico.ulisboa.pt

Instituto Superior Técnico, Universidade de Lisboa, Portugal

Dezember 2022

Abstract

Low altitude air flying vehicles, have emerged recently for cargo or even human transportation. It is of utmost importance to maintain the vehicle safe from collisions, specially when transportation of humans is considered.

In this work, a simulation of a radar system to identify targets in its surroundings is done, with emphasis in the design of the sensing component of the system (the antenna). The design of a square microstrip patch antenna (being versatile in terms of resonant frequency), of a planar antenna array with main lobe steering capability (being versatile in terms of main lobe beam width), and of a target detection method for the radar (being versatile in terms of target identification sensibility) are done.

The transmission line and cavity models are used to compute the dimensions of the square microstrip patch antenna. The antenna used throughout this work was designed at 35 GHz, being fed to radiate dual linear polarized waves, to minimise the probability of missing targets due to polarization mismatch.

The optimized square microstrip patch element is used on a Dolph-Chebyshev planar array, also square, with 8x8 elements. This type of array provides the lowest side lobe level, for the defined beam width, as required in radar applications. The main lobe can be scanned up to 45° from broadside.

The concepts are validated using a simulation method, based on images taken from a 3D environment, with the purpose of identifying the targets positions relative to the system. A long range and a short range scenarios are tested.

Keywords: AAV, UAV, microstrip patch antennas, dual linearly polarized patch antenna, Dolph-Chebyshev arrays, planar arrays, beam steering, mm-wave radar, radar signal simulation

1. Introduction

A Radar system works by transmitting electromagnetic waves that propagate in free-space and reflect in objects along their path. An antenna is one of the main components of a Radar system, being used to convert the energy from a guided wave to the free-space wave, and vice-versa. When transmitting, the antenna transfers the electromagnetic signal at carrier frequency to the free-space, and when receiving it collects the reflected signal from the target. A Radar system can have a wide area of applications depending on its type, that is defined based on the antenna characteristics. In this work, a narrow beam low side lobe level Radar system is designed, with the purpose of mapping the objects located in an environment.

In a Radar system, by receiving the echo signal, besides claiming or not the detection of a target, it is also possible to calculate its distance, by analysing the time delay between the transmitted and received signal, and relative radial velocity, by analysing the frequency shift of the reflected wave caused by the Doppler effect [1]. A Radar cannot resolve as much detail as other type of sensors available nowadays, and it is costlier to manufacture, but has the advantage of being capable of providing reliable information under adverse environmental conditions, in which the others cannot [1], thus being essential for a more reliable safety system of air vehicles.

In this work, the Radar data will be simulated using *Blender* software to define a 3D environment, with a post-processing phase in *Python* using the camera rendered image to simulate the radar signal of a system, using the previously designed array. The data obtained from the Radar can even be stored and mapped to a 3D construction model, according to the system position and orientation related to a local coordinate system.

2. Background

2.1. Microstrip Patch Antenna

The desired frequency was to be set within the mm-Wave frequency (EHF band), which have a few propagation characteristics to take into ac-

count when designing a highly directive radar, such as higher path loss and atmospheric absorption [2]. The free-space path loss decays with the square of the transmitted frequency, and it's the principal source of power loss in mm-Wave Radars. The atmospheric attenuation is the second major source of power loss in mm-Wave Radars, and to minimize it, the frequency was set to 35 GHz, which has nearly the minimum attenuation for the frequency band $f \in [30, 60]$ GHz [3].

An initial estimation for the patch width W, is given by equation 1. Note that the wavelength $\lambda_0 = \frac{c}{f_r}$, and ϵ_r is the effective dielectric constant, given by equation 2.

$$W = \frac{\lambda_0}{2}\sqrt{\frac{2}{\epsilon_r + 1}} \tag{1}$$

$$\epsilon_{reff} = \frac{\epsilon_r + 1}{2} + \frac{\epsilon_r - 1}{2}\left[1 + \frac{12h}{W}\right]^{-1/2}, \quad W \geq h \tag{2}$$

Fringing is a well known effect that happens due to the nature of patch antennas, that creates a non-homogeneous electrical path between two dielectrics (the air and the substrate). Due to fringing, electrically the patch looks larger than its physical dimensions, phenomena that affects the resonant frequency of the patch. As the height of the substrate increases, fringing also increases [4]. The effective length of the antenna is given by $L_{eff} = \frac{\lambda_g}{2} = \frac{\lambda_0}{2\sqrt{\epsilon_{reff}}}$. The effective length of the patch L_{eff} is given by $L_{eff} = L + 2\Delta L$, being L is the physical length of the patch. The extension along the length of the antenna ΔL is a function of ϵ_{reff} and of the ratio W/h, given by:

$$\Delta L = 0.412h\frac{(\epsilon_{reff} + 0.3)(\frac{W}{h} + 0.264)}{(\epsilon_{reff} - 0.258)(\frac{W}{h} + 0.8)} \tag{3}$$

Since the patch dimentions are in the mm range, a direct feed from the coaxial cables to the patch is a very rigorous task, and is prone to error. Even if higher impedance coaxial cables, which are thinner, were to be used, since the patch would need two independent coaxial cables to achieve dual linear polarization, the cables would be extremely close in distance. Thus, a coaxial cable will be connected to a microstrip line that is matched with a quarter wavelength transformer to feed the border of the patch. A quarter wavelength transformer is depicted in figure 1, being the impedance of the transformer given by equation 4.

$$Z_2 = \sqrt{Z_1 Z_3} \tag{4}$$

The goal is to achieve dual-linear polarization in the final antenna. Assuming that the vertical polarization happens when the patch is fed at a border

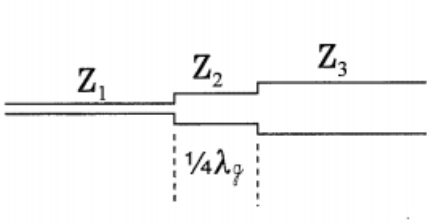

Figure 1: Quarter wavelength transformer

along its width (x-axis), the dominant mode will be the TM_{010}, and mode TM_{100} will be dominant for the horizontal polarization, which happens when the patch is fed at the border along its length (y-axis), as depicted in figure 5. The resonant frequency for each polarization have an inversely proportional relationship with the width and length of the patch, and can be tweaked according to the following equations:

$$\begin{aligned}(f_r)_{vertical} &= \frac{\pi}{2\pi L\sqrt{\epsilon_{reff}}\sqrt{\mu_0\epsilon_0}} \\ (f_r)_{horizontal} &= \frac{\pi}{2\pi W\sqrt{\epsilon_{reff}}\sqrt{\mu_0\epsilon_0}}\end{aligned} \tag{5}$$

2.2. Antenna Array

The array factor **A(**θ, ϕ**)** of an N-element array is a function of the weights a_n (which define the type of excitation) and position of each element, being defined in equation 6. An uniform array has equal weights a_n for all antennas, meaning that each antenna radiates an equal amount of power. Note that **k** is the propagation vector in the direction of the field vector.

$$\mathbf{A}(\theta, \phi) = \sum_{n=1}^{N} a_n e^{j\mathbf{k}\cdot\mathbf{d}_n} \tag{6}$$

Furthermore, the gain of the array $G_{total}(\theta, \phi)$ is related to the gain of the single element $G(\theta, \phi)$ by the power gain of the array $|\mathbf{A}(\theta, \phi)|^2$, being given by equation 7.

$$G_{total}(\theta, \phi) = |\mathbf{A}(\theta, \phi)|^2 G(\theta, \phi) \tag{7}$$

The propagation constants k_x, k_y and k_z, corresponding to the x, y, and z axis are given by:

$$\begin{aligned}k_x &= k_0\sin(\theta)\cos(\phi) \\ k_y &= k_0\sin(\theta)\sin(\phi) \\ k_z &= k_0\cos(\theta)\end{aligned} \tag{8}$$

The angular dependence of the array factor comes through the propagation constant k_x, k_y or k_z [5]. Simplifying the design by setting the same inter-element spacing d leads to define an auxiliary variable in the wavenumber space ψ:

$$\psi = \mathbf{k} \cdot d, \tag{9}$$

and the array factor from equation 6 can be written in terms of ψ as follows:

$$A(\psi) = \sum_{n=0}^{N} a_n e^{jn\psi} \tag{10}$$

The array factor $A(\psi)$ is periodic in ψ with period 2π, however, the true range of ψ that affects the physical behaviour of the array is named the visible region, and is defined as the interval $\psi \in [-kd, kd]$. In case the visible region is bigger than the period of $A(\psi)$, the values of the array factor repeat in the visible region, and secondary main lobes (*grating lobes*) arise at different directions than the desired one [5].

The size of the visible region also affects the directivity of the array. An array with N elements will have $N-1$ zeros that will correspond to nulls in the radiation pattern. In order to achieve the maximum directivity and avoid grating lobes, the visible region should reach the last null before the main lobe of the following period in ψ [6].

The Dolph-Chebyshev excitation provides a definition of the window $w(m)$ such that the main lobe directivity is optimized for a given side lobe attenuation. The window $W(\psi)$ for the Dolph-Chebyshev array is related to the Chebyshev polynomials of first kind $T_{N-1}(x)$, defined in equation 11, with x_0 being the scale factor.

$$W(\psi) = T_{N-1}(x), \qquad x = x_0 \cos(\frac{\psi}{2}) \tag{11}$$

The Dolph-Chebyshev window $W(\psi)$ is defined such that the main lobe corresponds to a portion of the Chebyshev polynomial in the region where $x > 1$ and the side lobes correspond to a portion of the polynomial in the region where $|x| \leq 1$. The Chebyshev polynomials of the first kind are defined in equation 12.

$$T_m(x) = \begin{cases} \cos(m \cdot \arccos(x)), & if\ |x| <= 1 \\ \cosh(m \cdot \operatorname{arccosh}(x)), & if\ |x| > 1 \end{cases} \tag{12}$$

The interval $[x_{min},\ x_0]$ can be split into two subintervals, $[x_{min},\ 1]$ and $[1,\ x_0]$, corresponding to the side lobe and main lobe interval of the array factor, respectively. For an angle $\phi \in [0°,\ 180°]$, the wavenumber $\psi = kd\cos(\phi)$ will range over the visible region. The quantity x will start at the value of x_{min}, and after it reaches the value of x_0, which corresponds to having $\phi = 90°$, x will move back until it reaches the value of x_{min} again, making the zeros of the Chebyshev polynomial the zeros of the array factor at each side of the main lobe, as depicted in Figure 2.

The value of $W(\psi)$ at $x = x_0$ correspond to the relative side lobe attenuation level in absolute units [6]. The scale factor x_0 is always greater than 1, and thus, the window W_{main} at $\psi = 90°$ or $x = x_0$ is defined as:

$$W_{main} = \cosh((N-1) \cdot \operatorname{arccosh}(x_0)) \tag{13}$$

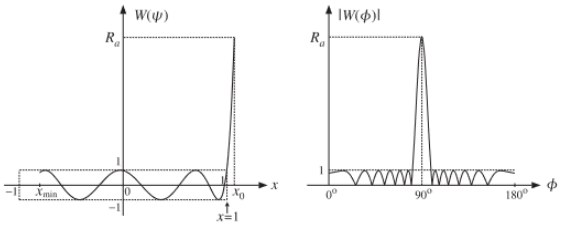

Figure 2: Chebyshev polynomials to array factor in wavenumber-space (extracted from [6])

The side lobe level of the array is given by $R_a = \frac{W_{main}}{W_{side}}$, with $W_{side} = 1$.

The following relation allow to design the array by defining the desired side lobe level atenuation:

$$x_0 = \cosh(\frac{\arccos(R_a)}{N-1}) \tag{14}$$

The Dolph-Chebyshev window function $w(m)$ is obtained by computing the z-transform of the computing the inverse z-transform of the z-transform of the array factor, constructed from its zeros. In the region of the $N-1$ zeros, the window $W(\psi)$ is defined as:

$$W(\psi) = \cos((N-1) \cdot \arccos(x)) \tag{15}$$

The the $N-1$ zeros x_i of $W(\psi)$ are found to be:

$$x_i = \cos(\frac{(i-1/2)\pi}{N-1}), \quad i = 1, 2, ..., N-1 \tag{16}$$

Solving for each wavenumber using $x_i = x_0 \cos(\psi_i/2)$, the pattern zeros ψ_i are obtained:

$$\psi_i = 2\arccos(\frac{x_i}{x_0}) \tag{17}$$

Being each pattern zero represented in the z-space as $z_i = e^{j\psi_i}$. The symmetric z-transform of the window $W(z)$ is constructed with equation 18.

$$W(z) = z^{-(N-1)/2} \prod_{i=1}^{N-1} (z - z_i) \tag{18}$$

The inverse z-transform of 18 gives the window coefficients normalised to unity, that differ from the ones in equation 10 by the scale factor $\frac{x_0^{(N-1)}}{2}$.

As a further simplification to describe the steering capabilities of an array, consider the array symmetrical along the x-axis, such that the array factor

is measured along ϕ. Its maximum is $A(0)$, which corresponds to $\psi = k_0 d\ cos(\phi) = 0$ or $\phi = 90$. By applying a phase shift between consecutive antennas, the maximum of the array factor will be steered towards a certain angle ϕ_0. The corresponding steering phase ψ_0 to be applied between consecutive elements is given by

$$\psi_0 = k_0 d \cos(\phi_0) \tag{19}$$

Figure 3 illustrates the difference on the array factor for a beam steered towards ϕ = 90º or towards another arbitrary angle.

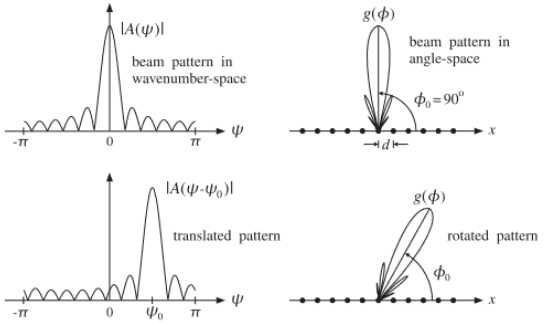

Figure 3: Non-steered vs steered patterns (extracted from [5])

The translated digital wavenumber is defined as $\psi' = \psi - \psi_0$ and the steered array factor is given by:

$$A'(\psi) = A(\psi - \psi_0) \tag{20}$$

The weights coefficients for each antenna of the steered array are defined as

$$a'_n = a_n e^{-j\psi_0 n} \tag{21}$$

being ψ_0 the phase shift between consecutive elements and a_n the weight of the non-steered array.

For the steered array, the visible region shifts accordingly to the angle ϕ_0. The visible region is defined in the wavenumber-space as the phase shift ψ_0 in the interval

$$\psi_0 \in [-kd(1 + \cos(\phi_0)),\ kd(1 - \cos(\phi_0))] \tag{22}$$

and to ensure that no grating lobes exist, the maximum spacing between elements d must be:

$$d_{max} = \frac{\lambda}{1 + |\cos((\phi_0)_{max})|} \tag{23}$$

2.3. mm-Wave FMCW Radar

The signal $S_{Tij}(t)$ to transmit through each antenna in the array is given by equation 24, being the total power transmitted by the array P_t, given by equation 25. Note that a_{ij} and ψ_{ij} are the gains and phase shift of each antenna, respectively.

$$\begin{aligned} S_{Tij}(t) &= (\sqrt{2a_{ij}P_{t0}})e^{j(2\pi \cdot f(t) - \psi_{ij})} \\ &= (\sqrt{2P_{Tij}})e^{j(2\pi \cdot f(t) - \psi_{ij})} \end{aligned}, \quad t \in [0, T_{ch}] \tag{24}$$

$$P_t = \sum_{i,j} P_{Tij} \tag{25}$$

With a single radiation pattern, the radar system propagates power in different directions, being the received signal affect by targets in every direction. The signal received by a radar system is given by equation 26, being the power of the received signal computed using equation 27.

$$S_r(t) = \sqrt{2P_r} G_{LNA} e^{-j2\pi f_b t} + w(t) \tag{26}$$

$$P_r = \frac{P_t G(\theta, \phi)^2 \lambda^2 \sigma \Gamma}{(4\pi)^3 R^4} \tag{27}$$

The instantaneous difference in frequency between the transmitted and received signals, named the beat frequency f_b, is related to the target distance, being given by equation 28, and is graphically represented in figure 4 [7].

$$f_b = \frac{2R}{c} \cdot \tan(\alpha) = \frac{2RB_{ch}}{cT_{ch}} \tag{28}$$

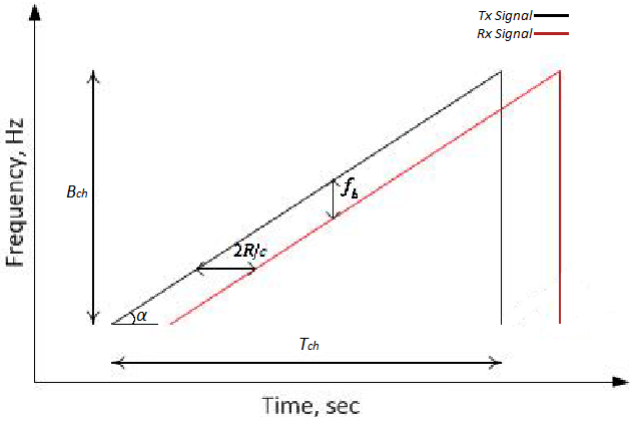

Figure 4: Frequency vs time - Transmitted vs Received Signals (extracted from [7])

The signal shall be sampled at N points, considering the maximum frequency to detect, based on the Nyquist frequency [8]. To perform detection algorithms, the amplitude of the sampled signal must be computed from the Fast Fourier Transform (FFT) $X(k)$, according to equation 29. Note that $\max(|X(k)|) = \max\left(\sqrt{Re\{X(k)\}^2 + Im\{X(k)\}^2}\right)$.

$$A_{fft} = \frac{2 \cdot \max(|X(k)|)}{N} \tag{29}$$

The target detection operation asserts if the amplitude of the sampled signal is under a threshold level V_{th}, being the following criteria is used:

$$\begin{cases} A_{fft} < V_{th}, & \text{target absent} \\ A_{fft} > V_{th}, & \text{target present} \end{cases} \quad (30)$$

The value threshold voltage V_{th} is usually chosen using the Neyman-Pearson criteria, given by equation 31, being σ_N the noise variance, and P_{fa} the false alarm probability, a common characteristic of radar systems [9].

$$V_{th} = \sqrt{-2\sigma_N^2 \ln(P_{fa})} \quad (31)$$

3. Methodology

3.1. Microstrip Patch Antenna

The physical dimensions for the microstrip patch antenna were obtained by reiterating the process described between equations 2 and 3, with $W = L$ at the end of each iteration, until both dimensions to converge to a value, making the patch squared. The quarter wavelength transformer to connect each coaxial cable to the patch was dimensioned using equation 4.

The chosen substrate is RT/duroid 5880 with a dieletric constant of 2.20 ± 0.015 with a loss tangent @ 10 GHz of 0.0009. The antennas and transmission lines will be made of copper with $0.035\ mm$ of plate thickness. The substrate height is usually in the range of $0.003\lambda_0 \leq h \leq 0.05\lambda_0$. The desired patch resonant frequency is 35 GHz, thus the substrate height must be in the range $[0.0257, 0.4286]\ mm$. The patch was modelled with substrates of height 0.508 mm, 0.381 mm and 0.254 mm to evaluate its effect on the antenna properties.

By specifying the desired resonant frequency, the substrate dielectric constant and height, and the impedance of the coaxial cable, the width W, length L and impedance R_0 of the border of the patch, as well as the impedance of the quarter wavelength transformer to connect the coaxial cable to the border of the patch Z_{qwt} are computed. Then, the physical size of the antenna was optimised in the electromagnetic field simulation software $CST\ Studio\ Suite$.

3.2. Antenna Array

The *Matlab* "Electromagnetic Waves & Antennas" toolbox from [10] was used to create a script that simulates the theoretical radiation pattern and outputs the Dolph-Chebyshev weights for a linear array, given the desired number of elements N, inter-element spacing d, side lobe attenuation level Ra, and main lobe direction ϕ_0. The script was done according to the reasoning of section 2.2. Furthermore, the software $CST\ Studio\ Suite$ was used to optimise the array.

For the final array, d was set to $d = 0.5\lambda_0$. The distance between elements affects the visible region of the array, which have a direct effect on the array directivity. Using $0.5\lambda_0$ as inter-element spacing is a very common practice, and usually ouputs balanced results. The desired side lobe attenuation level was set to $R_a = 25$ dB to be suitable for Radar applications. The design was done considering the main lobe direction was set to $\phi_0 = 90°$, being ortogonal to the array plane. The radiation patterns obtained for the vertical and the horizontal polarization are proved to be very similar.

Once the planar array is validated with the main lobe orthogonal to the array plane, an analysis of its steering capabilities was done.

3.3. mm-Wave FMCW Radar Simulation

The Radar simulation is performed based on rendered images obtained from a 3D environment created in the open source software *Blender*. The 3D environment was setup in *Blender* by inserting objects into a scene. A camera is a special object that specifies to the ray tracer the part of the scene to be rendered into an image, having several properties that can be tweaked to achieve the desired characteristics for the output image. In *Blender*, the camera lens defines how the 3D environment is mapped to the 2D image, being a key property to control the image output projection.

To output the rendered image directly to a file, compositing was used in The "Render Layer" in *Blender* was exported, selecting the Z-pass and Normal-pass data to be output along with the image, into a $.exr$ format, which allows to have different data layers for every pixel in an image [11]. The Z-pass data contains the absolute distance in meters from the camera position to any visible surface within its field of view, and the Normal-pass contains the surface normal vector weights, relative to the main referential of the scene, both information being obtained for each pixel during the rendering done by the ray tracer.

The rendered images were output with panoramic fisheye equidistant, also known as tiny planet, projection. This is a type of stereographic projection, that maps the spherical view of the environment seen by the camera to a flat image, having a linear relation between its variables (r_{fep},θ_{fep}) and the latitude and longitude, respectively, of each point seen by the camera, when analysed with a polar coordinate system at its center [12]. Points at equal distance r_{fep} to the centre of the referencial all have the same latitude, and points at the same θ_{fep} all have the same longitude. The projection field of view was set to $180°$, covering half of the whole spherical image seen by the camera, and the image pixel resolution was set to $N_{pix} \times N_{pix}$ pixels. Assuming that the antenna array is located at the camera

position facing towards the environment seen in the image, it is possible, by using equations 32 and 33, to convert each pixel position (n_{px}, n_{py}) of the image with fisheye equidistant projection, to an angular direction (θ_{pos}, ϕ_{pos}) with $\theta \in [0°, 90°]$ and $\phi \in [0°, 360°[$, corresponding to the direction of that point in space relative to the antenna referential.

$$\begin{aligned} r_{fep} &= \sqrt{((\frac{N_{pix}}{2} - n_{px})^2 + (\frac{N_{pix}}{2} - n_{py})^2)} \\ \theta_{fep} &= \arctan\left(\frac{\frac{N_{pix}}{2} - n_{py}}{\frac{N_{pix}}{2} - n_{px}}\right) \end{aligned} \tag{32}$$

$$\begin{aligned} \theta_{pos} &= r_{fep} * \frac{90}{N_{pix}/2}, \quad n_{px}, n_{py} \in [0, N_{pix}] \\ \phi_{pos} &= \theta_{fep} \end{aligned} \tag{33}$$

An easy way to correlate the rendered images to the radiation patterns, is to map the exported data from each radiation pattern to an image with fisheye equidistant projection, and process the rendered image pixel by pixel, using each radiation pattern to simulate the scan of the antenna to each desired direction. Thus, an image with the same pixel resolution $N_{pix} \times N_{pix}$ shall be created for each radiation pattern. The images are filled by calculating the orientation (θ_{pos}, ϕ_{pos}) of each pixel using equations 32 and 33, and assigning the value of the gain in that direction of each radiation pattern untill all pixels are filled. Note that only pixels with $r_{fep} < N_{pix}/2$ shall be mapped, since the remaining pixels do not contain valuable data in a fisheye equidistant projection.

The calculated pixel point latitude and longitude $(\theta_{pos}, \phi_{pos})$, allow to calculate the unitary vector $\overrightarrow{r_{pos}^{ant}}$ in the pixel direction, relative to the antenna referential, using equation 34.

$$\overrightarrow{r_{pos}^{ant}} = \begin{bmatrix} \cos(\theta_{pos}) \cdot \cos(\phi_{pos}) \\ \cos(\theta_{pos}) \cdot \sin(\phi_{pos}) \\ \sin(\theta_{pos}) \end{bmatrix} \tag{34}$$

The camera axis in *Blender* is oriented such that every pixel in the image correspond to a point with a negative z-coordinate. Throughout this work, the Euler rotations are performed in the XYZ order, and thus, the used rotation matrix, R_{XYZ}, is represented in equation 35, with R_X, R_Y and R_Z being the Euler rotation matrices over each axis.

$$R_{XYZ}(\alpha_x, \alpha_y, \alpha_z) = R_Z(\alpha_z) \cdot R_Y(\alpha_y) \cdot R_X(\alpha_x) \tag{35}$$

The Z-pass data can be used along with each unitary vector to obtain the point position relative to each referential. Note that, to calculate the point position in the scene referential, the camera location $P_{cam} = (P_{camX}, P_{camY}, P_{camZ})$, exported along with the render, must also be taken into consideration. The surface point represented in the pixel (n_{px}, n_{py}) can be positioned in the coordinates of each referential, being the P_{pos}^{ant}, P_{pos}^{cam} and P_{pos}^{scene}, the coordinates of the location of that point in the antenna referential, in the camera referential and in the scene referential, respectively. This is easily computed using equations 36.

$$\begin{aligned} P_{pos}^{ant} &= Z_{pass}(n_{px}, n_{py}) \cdot \overrightarrow{r_{pos}^{ant}} \\ P_{pos}^{cam} &= Z_{pass}(n_{px}, n_{py}) \cdot \overrightarrow{r_{pos}^{cam}} \\ P_{pos}^{scene} &= \begin{bmatrix} P_{camX} \\ P_{camY} \\ P_{camZ} \end{bmatrix} + Z_{pass}(n_{px}, n_{py}) \cdot \overrightarrow{r_{pos}^{scene}} \end{aligned} \tag{36}$$

4. Results & discussion

4.1. Microstrip Patch Antenna

The results of the pre-design for the substrates with height $h = 0.508$ mm, $h = 0.381$ mm and $h = 0.254$ mm are depicted in table 1.

h (mm)	0.508	0.381	0.254
W = L (mm)	2.60	2.63	2.67
R_0 (Ω)	198.9	195.7	192.9
Z_{qwt} (Ω)	99.7	98.9	98.2
L_{qwt} (mm)	1.59	1.61	1.63
W_{qwt} (mm)	0.46	0.33	0.20

Table 1: Antenna simulation results for different substrate height

Three simple models were made and optimised on $CST\ Studio\ Suite$ to evaluate the radiation pattern for each substrate height. The substrate was modelled as 5 times bigger than the patch width and length, and the patches were fed using a $100\ \Omega$ coaxial cable that was modelled. The simulations lead to the following conclusions about the influence of the substrate height on the radiation pattern of the single element:

1. The substrate height highly influences the width of the transformer, and it is possible to verify its influence on the E-plane of the radiation pattern.

2. Without the influence of the transmission line, the directivity increases and the 3dB angular width decreases as the substrate gets thinner.

To minimise the effects of the transmission lines and to achieve a higher directivity the substrate with $h = 0.254$ mm was used for the final single element model, represented in figure 5. The antenna consists of the patch, two microstrip lines and two coaxial cables to control both polarizations. Both transmission lines are transforming the $50\ \Omega$ from

each coaxial to R_0 in order to avoid using inset feeds to keep the similarity of the radiation pattern between polarizations. Coaxial cables 1 and 2 are stimulated independently to obtain vertical and horizontal polarization, respectively. The xz-Plane corresponds to the H-plane of the vertical polarization and to the E-plane of the horizontal polarization, and the yz-Plane corresponds to the E-plane of the vertical polarization and to the H-plane of the horizontal polarization.

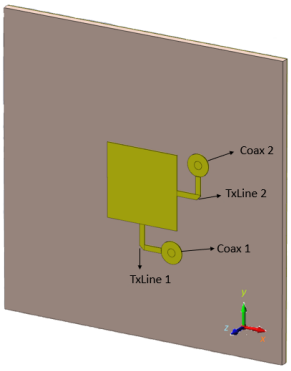

Figure 5: Dual linear polarized patch antenna

The simulation results showed that the impedance matching between the transmission line and the antenna is verified by the magnitude of the S-Parameter and by the Smith Chart at the frequency of operation (35 GHz). Thus, it is possible to conclude that the transmission line successfully transforms the $50\ \Omega$ from the load to the impedance of the border of the patch. It is seen the main lobe slightly steered in the E-plane, due to the influence of the transmission lines, that also radiate power.

The results regarding horizontal polarization showed that a good impedance match between the transmission line and the antenna is also verified for this polarization. Analogue to the results of the vertical polarization, the H-plane show the main lobe slightly deviated from broadside. Note that for both polarizations and/or designs, this steered angle will become unnoticeable after designing the array.

The antenna has a narrow bandwidth for both polarizations, which is an already known limitation of patch antennas [13]. The bandwidth of the array will be slightly larger than the bandwidth of the single element antenna. Considering that the bandwidth is the frequency range where $|S_{11}|$ is below -10 dB, the antenna bandwidth is approximately 1 GHz.

The mutual coupling between ports can be evaluated by analysing the scattering parameters $|S_{12}|$ and $|S_{21}|$. Any interference lower than -15 dB would be acceptable. The feeds are obtained well isolated, evidencing that the two polarizations could be stimulated independently.

4.2. Antenna Array

The simulation was done based on the Dolph-Chebyshev coefficients feed of the antennas of a linear array. The Dolph-Chebyshev coefficients for an array with 8 elements and $R_a = 25$ dB were computed, and are represented in table 2.

a_1	a_2	a_3	a_4	a_5	a_6	a_7	a_8
1.00	1.55	2.23	2.65	2.65	2.23	1.55	1.00

Table 2: Dolph-Chebyshev coefficients for a linear array with $N = 8$ and $R_a = 25dB$

A squared array with 8x8 elements was modelled, and is depicted in figure 6. A squared array is a linear array of linear arrays, and the side lobe levels have to be controlled for both axis of the array. Thus, the weights for each element should be influenced by the element position according to each axis, in order to have higher weights at the centre of the array and lower ones as closer the element gets to one of the 4 corner elements, which have unitary weights. This effect is represented conceptually along with the whole array in figure 6.

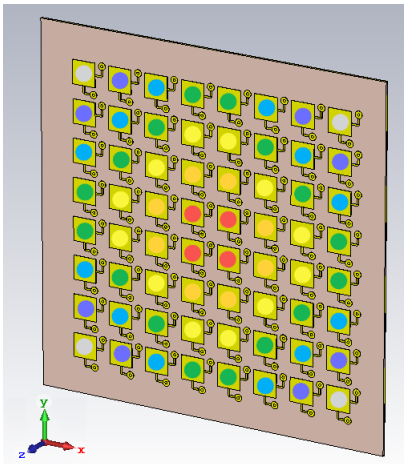

Figure 6: Squared array with 8x8 elements and conceptual feed weights technique

Considering the numbering from 1 to 8 of the elements from left to right in the x-axis, and top to bottom in the y-axis, the weight of each element can be referred as a_{ij}, with $i, j \in [1, 8]$. The weights for each element of the 8x8 array are related to the weights of the linear array in table 2 by equation 37.

$$a_{ij} = a_i \times a_j, \quad i, j \in [1, 8] \tag{37}$$

The simulation results showed that the magnitude of the reflection coefficient at the operating frequency is suitable for the desired purpose, and that the array achieved a bandwidth of approximately 1.5 GHz, from 34.3 to 35.8 GHz for the vertical polarization and from 34.2 to 35.7 GHz for the

horizontal polarization. A maximum reflection coefficient of -10 dB were considered for the bandwidth of the array.

The radiation pattern for vertical polarization and for the horizontal polarization of the squared array are nearly identical, as expected. The desired minimum side lobe levels are achieved for both polarizations. For the vertical polarization, the side lobe levels are -25.9 dB for the E-plane and -25.7 dB for the H-plane, along with a main lobe magnitude of 22.9 dBi for both planes and a Half-power Beam-width (HPBW) of $15.1°$ for the E-plane and $15.0°$ for the H-plane. Regarding horizontal polarization, the side lobes level are -25.5 dB for the E-plane and -25.8 dB for the H-plane, with a main lobe magnitude of 22.2 dB for both planes and a HPBW of $15.0°$ for the E-plane and $15.1°$ for the H-plane. The array was successfully stimulated with two different independent polarizations.

Furthermore, steering was accomplished. It is seen from the simulation results, that the Half-power Beam-width, side lobe levels and main lobe magnitude values were more affected as the steering angle increased. These values for the non steered pattern and for the steered patterns are represented in table 3

Desired main lobe direction [°]	0	15	30	45	60
ψ_0 [rad]	0	0.8131	1.5708	2.2214	2.7207
Obtained main lobe direction [°]	0	15	29	43	54
Main lobe magnitude [dBi]	22.9	22.4	21.8	21	20.3
Half-power Beam-width [°]	15	15.2	16.9	20	22.1
Side lobe level [dB]	-25.7	-24.9	-22.8	-20.9	-13.4

Table 3: Comparison between different steered radiation pattern characteristics

The purpose of this design is to steer the main lobe throughout the space where $z > 0$, (figure 6). To do so, a phase shift must also be applied between consecutive antennas in each row, making the phase of each element ψ_{ij} a function of its position within the array (figure 6), of the phase shift between elements in each line ψ_{0x} and in each row ψ_{0y}, defined by equation 38.

$$\psi_{ij} = i \times \psi_{0x} + j \times \psi_{0y}, \quad i, j = 1, ..., N \tag{38}$$

The simulations were done using the weights from table 3. It is possible to verify that the steering throughout the desired quadrant is accomplished, maintaining a minimum side lobe level of -20 dB for every steered radiation pattern. The main lobe HPBW increases as the steering angle in θ increase, which is a known limitation of phased arrays [14]. The phase shift combination $\psi_{0x} = 127°$ and $\psi_{0y} = 127°$ outputs the radiation pattern with characteristics that are affected by steering the most, being the obtained HPBW is $27.2°$, the main lobe magnitude 19.4 dB and a side lobe level of -20.6 dB.

4.3. mm-Wave FMCW Radar Simulation

The goal of the correlation between the rendered image and the radiation patterns, is to obtain the digital signal that would be sampled by the ADC of the radar system. The simulated signal, $S_{sim}(n)$ with N samples, was computed, for each radiation pattern, using equation 39, with $P_{r;px,py}$ and $f_{b;px,py}$ being the contribution of each pixel to the received power and to the beat frequency, respectively. The detection criteria was based on the frequency spectrum of the signal.

$$S_{sim}(n) = G_{LNA} \sqrt{2 \sum_{px,py} P_{r;px,py}} e^{-j2\pi f_{b;px,py} \cdot n T_s} \tag{39}$$

Two environments were made in $Blender$. Environment A consists of 3 cubes, placed at approximately the defined distance R_{max} from the camera position, and environment B consists on a mesh of objects, placed close to each other and close to the camera position. Note that the cubes all have the same size. Both images are taken with the camera at the same position and with the same orientation, being $(P_{camX}, P_{camY}, P_{camZ}) = (2, 0, 0)$m and $(\alpha_{camX}, \alpha_{camY}, \alpha_{camZ}) = (90, 0, 90)°$.

The radiation patterns obtained in section 4.2 were mirrored to the remaining quadrants. The radiation patterns were overlapped into an image, depicted in figure 7. Note that the simulation is done considering each radiation pattern individually, the purpose of figure 7 is just to visualise the whole area of the image scanned by the antenna.

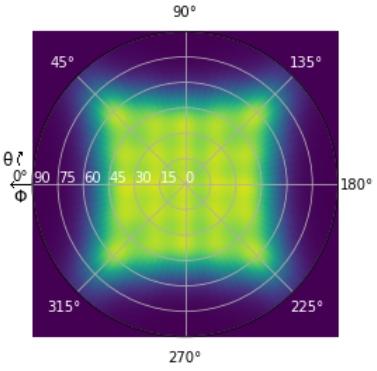

Figure 7: Area covered by the antenna array

The purpose of environment A was to verify that a target at approximately the maximum distance was detected, by obtaining a signal amplitude close to the detection voltage threshold. Only the cube positioned orthogonally to the camera was detected, obtained as result of the scan using the radiation pattern with mainbeam oriented orthogonally to the camera plane. However, it is possible to verify that, at a frequency corresponding to real distance, for both scans, the maximum

of the FFT occurs, being noticeable among the noise. This leads to the conclusion that if more power were transmitted, the targets would probably be detected. Furthermore, the cubes are not positioned directly according to the maximum of the considered radiation patterns, and the transmitted power was calculated using the maximum gain of the central radiation pattern, that has a higher gain compared to the ones in the remaining directions. Thus, there was a possibility that targets at directions in which the maximum gain of the antenna was lower than the one considered, would have a maximum detectable distance lower than the one defined. A similar environment was also created, considering the necessary distance to detect a target according to the objective of this work, in respect to the equivalent level of safety for see and avoid systems. The object was correctly identified.

The purpose of environment B was to verify that the radar system could identify a number of objects in its close vicinity, being the targets expected to be easily identifiable, with computed signal amplitudes much higher than the threshold level, since the targets are close to the camera. Targets were found in many directions. The environment seen in the rendered image and the result of the simulation are depicted in figures 8 and 9, respectively.

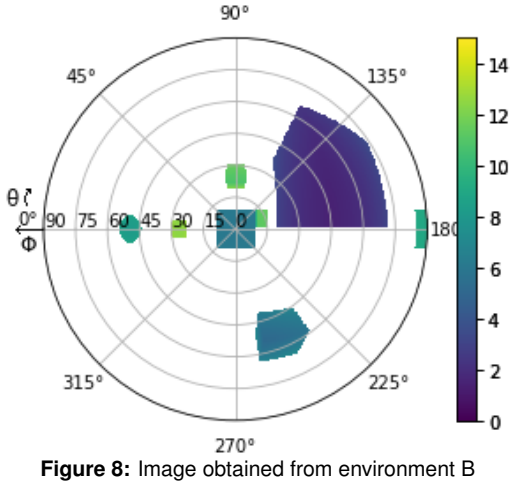

Figure 8: Image obtained from environment B

The results are obtained considered the distance computed from the frequency of the maximum of the frequency spectrum of each signal. However, it is noticeable in the frequency spectrums, that there are peaks lower than the maximum, but higher than the threshold level. These peaks correspond to a component on the sampled signal at different frequencies, being related to objects located at different distances that also reflected the transmitted signal. If these peaks were considered in the target detection phase, the radar could detect many objects in each direction, each positioned at the corresponding computed distance.

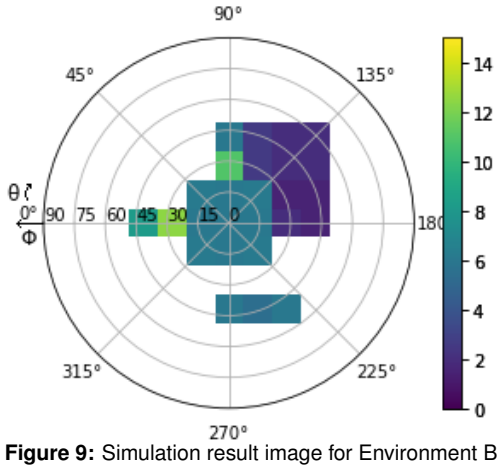

Figure 9: Simulation result image for Environment B

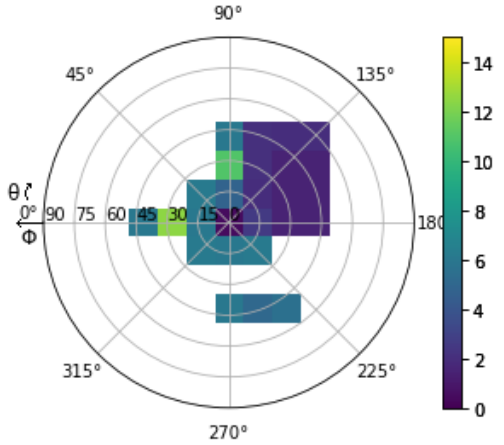

Figure 10: Simulation 2 result image - Environment B

For a safety system, it is of utmost importance that the system identifies the objects that are the nearest, in each direction. Thus, another simulation was done on environment B, considering that the detection was based on the first peak higher than the threshold level. This way, if many targets were detected by a scan, the closest one would be the one identified. The image result of the simulation is depicted in figure 10. It is noticeable, when comparing with figure 9, that some radiation patterns that identified the central cube, now identify the cube on the right, that is closest to the camera.

5. Conclusions

This work intends to contribute to the study and possible development of a safety system for low flying vehicles, with special attention given to Radar systems due to its reliability in different environment conditions. The theme was developed aiming to allow the definition of a complete configuration of the system according to the needs of the design, starting with the single antenna element, followed by the specification of the array and ending with the specification of the complete radar system.

The design of the patch antenna single element

was made using two well known models, the transmission line and cavity models. The physical size of the antenna was optimised using a eletromagnetic field simulation software tool. The result was a patch antenna that resonates at the desired frequency. The antenna should identify targets as reliably as possible, and since losing targets due to a polarization mismatch is a known phenomena [15], the antenna was designed with dual linear polarization, intended to output similar radiation patterns for both vertical and horizontal polarizations. By achieving this, the probability of missing a target detection due to polarization mismatch is decreased.

The antenna array used in a radar system is directly related to the detail of the objects identified, since its characteristics control the width of the mainbeam. The higher the angular resolution, the more angular directions can be scanned, the higher the gain, and the larger the distance of detectable targets. However, in order to avoid false detections, the sidelobe level of the array must be controlled. This was achieved using the well-known narrow-beam low side lobe level Dolph Chebyshev design, obtaining an array with the maximum possible gain for the desired side lobe level. Furthermore, the array mainbeam direction was controlled, providing steering capabilities, allowing to scan multiple directions with a fixed antenna. By achieving this, more angular directions can be accurately scanned.

The characteristics of the radar system are highly dependent on the working frequency of the used antenna. In this work, mm-Wave frequencies were considered, and a radar system suitable to be used with antennas optimised for this frequency band was studied. Since the production of such a radar is expensive, the validation of the system was done by simulating an environment with objects to be identified. By achieving this, it was proven the concept of using a highly directive radar to identify detected objects relative to its own position, data that could be used to prevent colisions of air flying vehicles.

References

[1] Merrill I. Skolnik. *The Nature of Radar*. McGraw-Hill Book Company, 1981.

[2] mmwave communication enabling techniques for 5g wireless systems: A link level perspective. In Shahid Mumtaz, Jonathan Rodriguez, and Linglong Dai, editors, *mmWave Massive MIMO*, pages 195–225. Academic Press, 2017.

[3] Tawfik Ismail, Erich Leitgeb, and Thomas Plank. Free space optic and mmwave communications: Technologies, challenges and applications. *IEICE Transactions on Communications*, E99.B, 2016.

[4] Constantine A. Balanis. *Microstrip Antennas*. John Wiley & Sons Inc., 1938.

[5] Sophocles J. Orfanidis. *Antenna Arrays*. Rutgers University, 2016.

[6] Sophocles J. Orfanidis. *Array Design Methods*. Rutgers University, 2016.

[7] Muhammad Z. Ikram, Adeel Ahmad, and Dan Wang. High-accuracy distance measurement using millimeter-wave radar. In *2018 IEEE Radar Conference (RadarConf18)*, pages 1296–1300, 2018.

[8] Robert Oshana. Overview of digital signal processing algorithms. In *DSP Software Development Techniques for Embedded and Real-Time Systems*, Embedded Technology, pages 59–121. Newnes, Burlington, 2006.

[9] Fernando D. Nunes. *Notes on Air Traffic Control Systems*. DEEC, Instituto Superior Técnico, Lisbon, Portugal, 2018.

[10] Sophocles J. Orfanidis. Electromagnetic waves and antennas.

[11] Openexr.

[12] Tiny planet algorithm? https://math.stackexchange.com/questions/607353/tiny-planet-algorithm. Accessed: 2022-08-20.

[13] Abdullahi SB. and Mohammed et al. Microstrip patch antenna: A review and the current state of the art. *Journal of Advanced Research in Dynamical and Control Systems*, 11(07-Special Issue):510–524, 2019.

[14] Mattia Rebato, Laura Resteghini, Christian Mazzucco, and Michele Zorzi. Study of realistic antenna patterns in 5g mmwave cellular scenarios. In *IEEE International Conference on Communications (ICC)*, pages 1–6, 2018.

[15] Mark A. Govoni, Jeffrey Spak, and Lee R. Moyer. Analysis of polarization mismatch loss for horizontal linear feature detection. Distribution A 2012.